Pro- and anti-oxidant properties of near-infrared (NIR) light responsive carbon nanoparticles.

Ida Kokalari,[a] Riccardo Gassino, [b] Andrea M. Giovannozzi, [c] Luca Croin,[c] Elena Gazzano,[d] Enrico Bergamaschi,[e] Andrea M. Rossi,[c] Guido Perrone,[b] Chiara Riganti,[d] Jessica Ponti[f], Ivana Fenoglio[a]*

[a] *Department of Chemistry, University of Torino, 10125 Torino, Italy.*
ivana.fenoglio@unito.it
[b] *Department of Electronics and Telecommunications, Politecnico di Torino, 10129 Torino, Italy*
[c] *National Institute of Metrological Research (INRiM), 10135 Torino, Italy*
[d] *Department of Oncology, University of Torino, 10126 Torino, Italy*
[e] *Department of Public Health and Pediatrics, University of Torino, 10126 Torino Italy*
[f] *Directorate F – Health, Consumers and Reference Materials Consumer Products Safety Unit (F.2), JRC, Ispra (Va), Italy*

Elemental carbon nanomaterials (ECNMs) are redox active agents that can be exploited to purposely modify the redox balance of cells. Both pro- or antioxidant properties have been reported. However, to the best of our knowledge, there are not comprehensive studies exploring both properties on the same material in view of a potential application in medicine. At the same time, the effect of the bulk structure on the pro/antioxidant properties is poorly known. Here, carbon nanoparticles (CNPs) derived by glucose with definite size and shape have been prepared, and their redox properties evaluated in cell free systems in the dark or following activation with a Near Infrared (NIR) laser beam (945 nm, 1.3 W/cm^2). We found that, when irradiated with NIR, CNPs efficiently generate heat and singlet oxygen ($^1O_2$), a property that can be exploited for dual photo-thermal (PT)/ photodynamic (PD) therapy in cancer. On the other hand, in the absence of photo-activation, CNPs react with both oxidant (hydroxyl radicals) and antioxidant (glutathione) species. When tested on a murine macrophages cell line (RAW 264.7) CNPs were clearly antioxidant. Furthermore, albeit efficiently internalized, CNPs do not exert cytotoxic effect up to 80 µg/ml and do not exacerbate TNF-α-mediated inflammation. Overall, the results reported herein suggest that CNPs may represent a new class of safe nanomaterials with potential applications in medicine.

Keywords: Reactive Oxygen Species • photodynamic • photothermal • carbon nanoparticles • hydrothermal carbonization

Introduction

Elemental carbon nanomaterials (ECNMs), a large family of different materials, are widely studied in medicine. Among them, the most interesting are those that contain π-π conjugated frameworks, in particular carbon nanotubes [1], graphene [2] or fullerene [3].

ECNMs are characterized by a rich chemistry that enables them as carriers for various therapeutic agents [4,5]. In addition, depending upon the bulk structure, some of these materials exhibit physical properties like fluorescence, photo-thermal (PT) and photodynamic (PD) capabilities that suggest a possible use as both therapeutic and diagnostic agents themselves. Photo-nanomedicine has gain significant attention as a branch of nanomedicine focused on the treatment of tumour [6] and other diseases such as infections [7]. It consists in employing nanoparticles (NPs) switchable by light in order to obtain a therapeutic effect. In fact, some NPs are able to strongly absorb light of a particular wavelength and convert it into sufficient heat to induce cell death, which is the principle of photo-thermal therapy (PTT). Nanomaterials including ECNMs, gold and iron oxides NPs are widely studied as PT agents [8]. Alternatively, other NPs generate highly cytotoxic Reactive Oxygen Species (ROS) through different mechanisms following light exposure. This therapeutic approach is referred as photodynamic therapy (PDT) [9]. The use of NPs as PD agents instead of light alone or molecules, typically porphyrins, increases efficiency and selectivity of the treatment if a selective uptake of the NPs in the target cells is achieved by passive or active targeting. In the last decade, numerous studies have explored the PT and PD properties of ECNMs [3] like fullerene, single wall carbon nanotubes, graphene oxide, with or without functionalization with light-sensitive molecules [10]. One advantage in using ECNMs in PT or PD therapies is that they are activated by near infrared (NIR) light. In fact, compared with UV or visible light, NIR radiations exhibit reduced autofluorescence [11], lower photo toxicity and deeper tissue penetration ability [8].

Several studies report that ECNMs are redox active species [12]. Both antioxidant and pro-oxidant properties have been described on the different materials [13,14]. These properties are highly relevant in cancer therapy. Cancer cells have level of ROS higher than normal cells. This has been related to tumour initiation, promotion and progression. At the same time, the increase of ROS concentration may activate pathways detrimental for tumour cells like apoptosis, necrosis and autophagy [15]. Therefore, several substances included ECNMs able to either suppress or promote

ROS, have been proposed as anticancer agents. Redox properties are also relevant for the safety of nanomaterials. In fact, an unbalance of the ROS level in healthy cells may activate inflammatory reactions or, on the contrary, may induce immunosuppression. In the case of ECNM, a comprehensive view on the effect of the various materials on cancer and healthy cells is still lacking. At the same time, while a wide number of studies suggest that the optical, thermal and redox properties of ECNMs are modulated by size, shape, surface and internal structure [16,17], the achievement of quantitative relationships between intrinsic and functional properties is still a challenge.

Saccharides-derived carbon nanoparticles are an emerging class of ECNMs. They have potential applications in several fields like adsorbents for heavy metals [18] or composites for energy storage [19], while some studies suggest a possible use also in medicine as nanoplatforms for theranostic applications [20–23]. Like other carbonaceous particles (soot, carbon black, etc.), they are substantially composed by amorphous carbon. However, they exhibit graphitic patches embedded in the amorphous matrix.

In the present study, a reproducible and high yield synthesis of CNPs derived by glucose (CNPs) of nanometric size has been achieved. The NPs have been studied for their bulk and surface properties and for their redox properties with or without photo-activation with a NIR laser beam in cell free systems. Finally, the capability of CNPs to modulate the redox homeostasis of macrophages was evaluated.

Experimental

Materials.

Carbon black (CB1) was obtained by oxidation in H_2SO_4/H_2O_2 solution of activated charcoal (Sigma-Aldrich, Germany). Carbon black (CB2) was a kind gift of Dr. Michela Alfé (Istituto di Ricerche sulla Combustione – CNR, Naples, Italy). Fullerene powder, hydroxylated, $C_{60}(OH)_n$, used as positive control in the generation of singlet oxygen, and 2,2,6,6-tetramethyl-4-piperidone monohydrate, 99% (TMP) were purchased from Alfa Aesar (Germany). Sodium polyacrylate, D(+)-glucose, thionine acetate salt, phosphate buffered saline powder, EDTA, glutathione reduced and 5,5'-dithiobis(2-nitrobenzoic acid) were obtained from Sigma-Aldrich (Germany). 5,5-dimethyl-1-pyrroline-N-oxide (DMPO) was obtained from Cayman chemicals

(USA). Ultrapure water was obtained from a Milli Q Plus system (Millipore, Bedford, MA, USA) and was always used freshly prepared. All other chemicals and solvents used were at least of analytical grade. When not otherwise specified, other reagents were purchased from Sigma-Aldrich.

Synthesis of glucose derived nanoparticles.

Preparation of carbon nanoparticles was achieved using the hydrothermal carbonisation method. Firstly, glucose in different amounts was dissolved in 50 ml of ultrapure water by magnetic stirring and sodium polyacrylate (15 mg) was then added in order to prevent the typical cross-linking of the nanoparticles during the synthesis. The solution was transferred in a Teflon-lined stainless-steel autoclave (100 ml, Büchi AG), and placed in a preheated oven at 190 °C for 3–8 h. The different synthesis conditions are summarized in Fig. 1a. After the synthesis, the nanoparticles suspension was concentrated, purified with ultrapure water by ultrafiltration using Vivaflow 50R cassettes (Sartorius, 30 kDa cutoff) and air dried at 70 °C for at least 48 h. The yields of the synthesis were calculated based on the mass of glucose used.

Morphological analysis.

Morphology studies of the CNPs samples, CB1 and CB2 were performed using scanning electron microscopy (SEM, QuantaTM 3D FEG DualBeamTM). In the case of carbon black samples, the samples were sputter coated by a thin layer of conductive metal (20 nm of AuPd) to prevent charging of the surface and to promote the emission of secondary electrons. The geometric diameter for CNPs samples was measured using the software ImageJ and expressed as mean of the diameter of up to 600 particles.

The optimized formulation was also analysed by high-resolution transmission electron microscopy (HRTEM). Micrographs were achieved with a 3010 Jeol instrument operating at 300 kV. Aqueous CNP suspension (0.05 mg/ml) was dropped on a copper grid covered with a lacey carbon film.

The mean hydrodynamic diameter and polydispersity index (PDI) of nanoparticles were obtained using a Zetasizer (Nano ZS Malvern Instruments) based on the dynamic light scattering (DLS) technique. The nanoparticles were suspended (1 mg/ml) in ultrapure water, sonicated (Bandelin Sonopuls HD 3100) and then diluted 1:5 in ultrapure water.

Thermogravimetric analysis.

Thermogravimetric analysis (TGA) was carried out in order to analyse the thermal stability of the nanoparticles and the presence of adsorbed species. The samples (ca. 3 mg) were placed in an open platinum pan which was supported by an ultra-microbalance (sensitivity 0.1 µg) and heated at a temperature range 35–700 °C at scan rate of 15 °C/min under N_2 (flow rate 35 ml/min) in a Pyris 1 TGA (PerkinElmer, MA, USA)

Raman spectroscopy.

For good sample homogeneity, CNPs were prepared as reported [24]. Briefly, 5 mg of powder were suspended in 1 ml of acetone (spectroscopic grade NVR ≤ 5%) and homogenized for 10 min in 80 W ultra-sonic bath at 15 °C temperature (Q700 Sonicator, QSonica). The solvent was allowed to evaporate up to 25% of the initial volume and the samples were homogenized again for 5 min in the same conditions. The suspensions were then transferred in a flat vial and completely dried in air (at least 2 h) before the characterization. Raman measurements were carried out using the Thermo Scientific DXR Raman confocal microscope system equipped with an excitation laser source at 532 nm, a full range resolution grating of 3 cm^{-1} with a spectral range from 50 to 3500 cm^{-1}, a 20x long working distance microscope objective, a 50 µm pinhole aperture and an automatic x, y motorized stage. Micro-Raman mapping was performed on each sample within an area of 400 μm^2 using a step size of 5 µm and collecting 25 spectra in total. Each spectrum of the map was registered with 1 s integration time and 70 scans. A low laser power of 1 mW was used to avoid thermal heating and any possible damage of the sample. The spectra of each the map were averaged and normalized to the band at about 1600 cm^{-1}. The curve fitting was performed with the combination of Gaussian–Lorentzian line shapes that gave the minimum fitting error. The structure and Raman spectra of carbonaceous materials can be interpreted in terms of highly disordered graphitic structures. However, these systems are radically different to any disordered carbon created from graphite and cannot be perfectly modelled by the Tuinstra-Koenig correlation [25], neither after the adjustments proposed by Ferrari and Robertson [26]. Therefore, the fitting models proposed by Sadezky et al., [27] and Li et al., [28] in the analysis of the Raman spectra from burned carbon and pyrolyzed coals, respectively, were preferred to deconvolute the Raman spectra of the CNPs here proposed.

ζ-potential.

Electrophoretic Light Scattering (ELS) technique was used to determine the zeta-potential of nanoparticles (Zetasizer Nano-ZS, Malvern Instruments, Worcestershire, UK) in the pH range from 2 to 10. An aqueous suspension of nanoparticles (0.8 mg/ml) obtained by probe sonication was diluted 1:3 with ultrapure water. The pH values of the resulting suspension were adjusted NaOH or HCl, 0.1 M or 0.01 M. The results are mean values of three experiments.

Quantification surface acidic groups density.

A spectrochemical titration assay, previously reported with modifications [29,30], was used for the quantification of surface acidic groups. The assay is based in the thionine acetate (THA) adsorption on the negatively charged moieties, which is responsible for the decolouration of the THA solution. CNPs (2 mg) were suspended in ultrapure water (1.875 ml) by ultrasonication and then an aqueous solution of THA (0.625 ml, 779.2 μM) was added. After 30 min of incubation under magnetic stirring in dark, the suspension was subjected to centrifugation (11.000 rpm for 30 min). The resulting supernatant was collected, filtered and its absorbance at 604 nm (Uvikon, Kontron Instruments, Inc., Everett, MA), due to the presence of the non-absorbed THA, was measured and compared with a calibration curve. The number of surface acidic functionalities was calculated assuming that THA reacts with acidic groups in stoichiometric ratio 1:1. The results are mean values of three experiments.

Evaluation of the photodynamic and photo-thermal properties.

The ability of the nanoparticles to generate singlet oxygen upon NIR irradiation was studied by EPR/spin trapping technique. Samples were prepared by mixing equal volumes of an aqueous suspension of CNP (4 mg/ml) and spin trap 2,2,6,6-tetramethyl-4-piperidone (TMP) solution (101 mM) in a quartz cuvette and then subjected to irradiation for 10 min at room temperature. A laser diode emitting a wavelength of 945 nm (1.3 W/cm^2) has been used as a light source. The laser light was conveyed through an optical fibre toward a lens adjusted in order to tailor the light spot dimension [30]. The potency of the laser was adjusted to a value normally used in PDT studies [31]. EPR spectra were measured on the suspension (Miniscope MS100, Magnettech,

Berlin, Germany). The negative control consisted of a TMP solution, while fullerenol $C_{60}(OH)_n$ was used as positive control for $^1O_2$ generation. In order to confirm the generation of singlet oxygen, the experiments were repeated after fluxing the suspension for 5 min with nitrogen (N_2) to remove dissolved oxygen and in the presence of 0.3 M NaN_3. During NIR exposure, it was also investigated the capability of the samples to convert the absorbed energy in heat by monitoring the temperature of the suspension by means of a glass optic fibre sensor, a Fibre Bragg Grating (FBG) [32], inscribed in a different fibre with respect to the delivery one. This was in real-time interrogated with a homemade system that provides the sample temperature every 0.5 s. This solution provides more accurate temperature estimation: since the fibre optic sensor does not absorb the laser light, the temperature is exactly the one of the solution.

Scavenging activity toward hydroxyl radicals.

The scavenging activity of CNP towards hydroxyl radicals was evaluated using electronic paramagnetic resonance (EPR)/spin trapping technique. 0.6 ml of a suspension of nanoparticles (5 mg/ml in phosphate buffer 0.5 M, pH 7.4) was transferred in a cuvette and stirred in the dark. 0.5 ml of a solution 0.15 M of 5,5-dimethyl-1-pyrroline N-oxide (DMPO) in water and 0.2 ml of a solution 13 mM of $FeSO_4$ were added. The reaction was started by adding 0.25 ml of a solution 0.2 M of H_2O_2. EPR spectra were measured on the suspension (Miniscope MS100, Magnettech, Berlin, Germany). The reaction was repeated in the absence of nanoparticles (control).

Reactivity toward glutathione.

The interaction of the samples with reduced glutathione was evaluated by a modified Ellman's assay [33]. The method is based on the reaction between 5 and 5'-dithiobis[2-nitrobenzoic acid] (DTNB, Ellman's Reagent) and GSH which lead to the formation of 412 nm chromophore, 5-thionitrobenzoic acid (TNB) and GS-TNB.

Samples were prepared mixing equal volumes of aqueous nanoparticles suspension (1 mg/ml) with a solution of reduced glutathione (GSH) (4 mM in EDTA 1 mM/PBS 0.1 M) and incubated for 2 h under shaking at 37 °C. The suspension was then subjected to centrifugation for 30 min at 11.000 rpm. The supernatant was collected and filtered. For the quantification of the residual

GSH, 100 µl of DTNB (4.3 mM in PBS 0.1 M/EDTA 1 mM) were added to the same volume of supernatant and the mixture was incubated for 5 min in the dark. The resulting solution was then diluted, and the UV–Vis spectra were recorded in the range from 200 to 600 nm (Uvikon, Kontron Instruments, Inc., Everett, MA). The concentration of residual GSH was calculated from a calibration curve. UV–vis spectra of the supernatant without Ellman's reagent were also acquired.

Cells.

RAW 264.7 murine macrophages were kindly supplied by Diana

Boraschi (CNR). Cells were cultured in Petri dishes in DMEM (Invitrogen Life Technologies, Carlsbad, CA) supplemented with 10% foetal bovine serum and 1% penicillin-streptomycin, then incubated in the same culture medium for 24 h, in the absence or presence of CNPs before the assays. A pyrogenic amorphous nanometric silica (Aerosil OX 50, Degussa Frankfurt A.M., Germany) was used as positive control. The protein content of cell monolayers was assessed with the bicinchoninic acid assay.

Particles dispersion in cell medium.

Nanoparticles stock suspension with a concentration of 1 mg/ml was sonicated for 30 min in a bath sonicator followed by vortexing in order to obtain a homogeneous dispersion. Aliquots of 1 ml were taken and sonicated with a probe sonicator (Bandelin Sonopuls HD 3100, Ti probe diameter 3 mm, power 400 W, frequency 20 kHz) for 2 min using the pulsation mode at 40% of power. The final suspension was then diluted in cell culture media at the desired concentrations. The stability of the suspensions was evaluated by Dynamic Light Scattering (DLS, Zetasizer Nano ZS, Malvern Instruments).

Measurement of lactate dehydrogenase leakage.

The cytotoxic effect of the nanoparticles was measured as the leakage of lactate dehydrogenase (LDH) activity into the extracellular medium, using a Synergy HT microplate reader (Bio-Tek Instruments, Winooski, VT), as previously described [34]. Both intracellular and extracellular LDH

were measured and then extracellular LDH activity (LDH out) was calculated as a percentage of the total (intracellular + extracellular) LDH activity (LDH tot) in the dish.

Purified LDH (from bovine muscle, purity > 99.5%) was used to rule out the interference of CNPs on the enzyme activity [35]. Briefly, cell culture medium in the absence (control) or presence of nanoparticles (10–320 µg/ml) was incubated with 0.3 U/ml of LDH at 37 °C. After 24 h, the medium was centrifuged, and enzyme activity was measured spectrophotometrically in the supernatants. Incubations up to 80 µg/ml of CNPs did not reveal any interference in agreement with what previously found on carbon nanotubes [35] (data not shown). A negligible effect was observed above the concentration of 160 µg/ml.

Uptake and Intracellular distribution.

The cellular uptake and distribution of CNPs was qualitatively evaluated by TEM analysis. RAW 264.7 murine macrophages were incubated for 24 h with 40 µg/ml and for 48 h with 160 µg/ml of CNPs. At the end of exposure, cells were washed, detached and re-suspended in 2% Karnovsky solution. Before analysis, Karnovsky solution was removed and cells re-suspended in osmium tetroxide solution in 0.1 M cacodilate pH 7.3 for 1 h. After three washes in cacodilate, 0.05 M of 10 min each, cells were dehydrated in a series of ethanol solutions in MilliQ water (30%; 50%; 75%; 95% for 15 min each, and 100% for 30 min), incubated in absolute propylene oxide for 20 min and embedded in a solution of 1: 1 epoxy resin -propylene oxide for 90 min. This mixture was renewed with pure epoxy resin over night at room temperature and later polymerized at 60 °C for 48 h. Ultrathin sections (50–70 nm) were obtained using Leica UCT ultramicrotome (Leica, Italy) and stained for 25 min with uranyl acetate and lead citrate for 20 min, washed and dried. Ultrathin sections were collected on Formvar Carbon coated 200 mesh copper grids (Agar Scientific, USA) and imaged by JEOL JEM-2100 h-transmission electron microscope at 120 kV (JEOL, Italy).

Measurement of Reactive Oxygen Species.

RAW 264.7 cells were incubated for 24 h in the absence or presence of CNPs, then cells were incubated for 30 min with 10 µM 2´,7´-dichlorodihydrofluorescein diacetate (DCFH-DA), as previously described [36]. DCF fluorescence was determined using a Synergy HT microplate

reader at an excitation wavelength of 504 nm and an emission wavelength of 529 nm. The fluorescence value was normalized to protein concentration and expressed as units of arbitrary fluorescence.

The experiments were repeated by adding 1 μg/ml of lipopolysaccharide (E. Coli 055:B5, Sigma-Aldrich) (LPS).

Measurement of nitrite.

RAW 264.7 cells were cultured for 24 h in the absence or presence of CNPs. The amount of extracellular nitrite (the stable derivative of nitric oxide) was measured spectrophotometrically, by adding 0.15 ml of cell culture medium to 0.15 ml of Griess reagent in a 96-well plate. After 10 min of incubation at 37 °C in the dark, the absorbance was detected at 540 nm with a Synergy HT microplate reader. For each experiment, a blank was prepared in the absence of cells, and its absorbance was subtracted from that measured in the presence of cells. Nitrite concentration was expressed as nmol nitrite/mg cell proteins.

Measurement of intracellular glutathione.

Intracellular reduced glutathione (GSH) was measured as previously described [34]. The kinetics of reaction was followed at 415 nm for 10 min using a Synergy HT microplate reader.

Each measurement was made in triplicate, and results were expressed as nmolGSH/ milligram cellular proteins.

Cytokine measurement.

Tumour necrosis factor-α (TNF-α) and interleukin-10 (IL-10) were measured in the supernatants of RAW 264.7 cells using the Mouse TNFalpha DuoSet ELISA (R&D Suystems, Mineeapolis, MN) and the murine IL-10 ELISA kit (PeroTech Inc., Rocky Hill, NJ), as per manufacturer's instructions. The results were expressed as pg cytokine/mg cellular proteins.

The experiments were repeated by adding 1 μg/ml of LPS.

Statistical analysis.

All data in the text and figures are provided as means ± SD. The results were analysed by a one-way analysis of variance (ANOVA) and Tukey's test. p < 0.05 was considered significant.

Results and discussion

Synthesis and characterization carbon nanoparticles (CNP).

Since the first study reporting the identification of carbon NPs as product of hydrothermal carbonisation of saccharides [37], different attempts have been made to exploit this process in order to develop CNPs with specific morphological characteristics. Spherical CNPs were previously obtained by glucose [38]. However, cross-linking among particles during the synthesis may occur [39]. To overcome this drawback, Gong et al. proposed the addition in the reaction mixture of the polymer sodium polyacrylate [40].

To establish the optimal synthesis conditions for the preparation of NPs with the desired size range, here we modified the original parameters of theprotocol proposed by Gong et al. in order to prepare NPs having diameter lower than 100 nm. The effects of the explored synthetic parameters are summarized in Fig. 1a.

A comparison between the mean hydrodynamic diameter (in number distribution) measured by dynamic light scattering and geometric diameter derived from SEM images is shown in Fig. 1b. The data confirmed that all the particles obtained were in nanosize ranges with a mean diameter that varies from 100 to 700 nm depending on the synthesis parameters. The high standard deviation in the mean geometric diameter of CNP1 is related to the presence of a very small population of NP having a diameter around 100 nm that can be observed in the SEM images but not during the DLS measurement, as the latter overestimates the larger particles. The morphology of NPs was evaluated by scanning electron microscopy. Fig. 1c shows typical SEM images of the different CNP. The NPs were all smooth and almost perfectly spherical in shape with a narrow size distribution. The yields of the synthesis after purification were 5,22,20% and 3% for CNP1, CNP2, CNP3 and CNP4, respectively, correspondent to 60–900 mg of product per synthesis. The polydispersity index for all the samples was below 0.15 (data not shown), further confirming that in all cases narrowly dispersed NPs were obtained [41]. The sample having the

lowest diameter (CNP4) was chosen for further characterization being the more promising candidate in therapy. In fact, different studies concerning spherical particles, confirm that a diameter of 50 nm seems to be the most favourable size in order to reach the highest cellular uptake of nanoparticles in tumour cells [42].

The synthesis was repeated several times to investigate the reproducibility. The hydrodynamic diameters and polydispersion indexes of the different batches are reported in Fig. S1, Supplementary material (SM). A representative image of the purified suspension of CNP4 is reported in Fig. S2, SM. The particles appeared composed by carbon (83.51%) and oxygen (16.49%), as revealed by EDS analysis (data not shown).

The bulk structure of CNP4 was investigated by high resolution TEM. A typical TEM image of CNP4 is shown in Fig. S3, SM. The nanoparticles appear spherical in shape confirming what observed by SEM, and with a low contrast, in agreement with a structure mainly composed by amorphous carbon. However, by high magnification, crystalline domains embedded in the amorphous structure of the nanoparticles were observed (inset). In the crystalline domains, the measured interlayer spacing was equal to 0.344 nm, a value that suggests the presence of turbostratic graphite.

The bulk structure of CNP4 was further investigated by Raman spectroscopy, a technique largely used [43–45] to provide information on the degree of ordering and crystallinity of carbonaceous materials [26–28]. In a high order single crystal graphite, Raman spectrum shows one band at around 1585 cm^{-1}, i.e. the G (''Graphite'') band, only, corresponding to an ideal graphitic lattice vibration mode with E2g symmetry. In case of polycrystalline graphite and disordered graphite systems, Raman spectrum exhibits additional first-order bands (D or ''Defect'' bands), whose most intensive is the D1 band, which appears at around 1360 cm^{-1} and corresponds to a graphitic lattice vibration mode with A1g symmetry. The D peak is due to the breathing modes of sp^2 atoms in rings and it grows in intensity relative to the G band with increasing degree of disorder in the graphitic structure. Few other second order modulations may be present in the range from 2300 cm^{-1} to 3300 cm^{-1} [46,47].

The analysis was performed in comparison with two samples of carbon black (CB1, CB2) having different degree of crystallinity, both composed by nanoaggregates, as shown in the SEM images in Fig. S4, SM, and with a specific surface area (details in methods, SM) equal to 58 m^2/g, for

CB1, and 196 m^2/g, for CB2. The Raman spectra of CB1, CB2 and CNP4 and the deconvolution patterns are shown in Fig. 2a. A full list of the picks of each spectrum is reported in SM, Table S1. The D and G bands dominate the first-order spectrum of CB1. The peak at ~1585 cm^{-1} comprises not only the G but also the D2 band known from disordered graphitic lattices. The valley between the two peak maxima can be attributed to another band at ~1530 cm^{-1}, which has been designated as D3 or A band in several studies [27,48,49], that originates from the amorphous carbon fraction of soot and aromatics with 3–5 rings. Two peaks due to overtones were also observed in the 2000–3000 cm^{-1} region further supporting the high degree of graphitization of this sample (Fig. S5, SM).

G and D bands were also observed in the Raman spectrum of the CB2 sample. However, a broadening of the G and D bands with respect to the ones of the CB1 together with an increase of the intensities of the signals related to amorphous carbon bands (1530 cm^{-1}, 1455 cm^{-1}, and at 1245 cm^{-1}) was observed [50]. All these features reveal a lower degree of graphitization and the related increase in structural disorder in the CB2 with respect to CB1. Moreover, it is important to note that the G band moved away from the position typical of the graphite at 1585 cm^{-1} and shifted towards ~1600 cm^{-1}. This shift was previously observed in other studies [49,51]. No significant signals were observed in the second order region of the Raman spectrum.

Raman spectrum of CNP4 shows a higher level of noise and a different background slope compared to the spectra of the other samples. We infer that this behaviour was mainly due to the photoluminescence of the CNP, as confirmed by fluorescence measurement (see hereafter). The amorphous carbon content in this sample was indicated by the broad and overlapping bands across the spectrum. The G band does not only comprise the peak at ~1585 cm^{-1} but also the D2 band known from disordered graphitic lattices at ~1620 cm^{-1}. D band, not very well defined, seems to be centred at 1300 cm^{-1}. This suggests that it mainly arises from larger aromatic features with six or more fused rings [27]. The overlap between D and G bands was deconvoluted into three bands at ~1550 cm^{-1}, at 1425 cm^{-1} and 1370 cm^{-1} which represent typical structures in amorphous carbons (especially smaller aromatic ring systems) as well as the semicircle "breathing" of aromatic rings [49]. Few other bands were observed in the present spectrum: the D4 band at 1145 cm^{-1} and the peak at ~1200 cm^{-1}, that were previously assigned to sp^2-sp^3 bonds with C–C and C=C stretching vibrations of polyene-like structures and to the

aryl-alkyl ether respectively, and the bands at 1030 and 1840 cm^{-1}, previously attributed to oxygen-related functional groups [37].

In order to confirm the assignment of the Raman shifts observed for CNP4, thermal annealing at 700 °C was performed. As expected, the Raman analysis (Fig. S6, SM) revealed, together with a reduction of the spectral noise due to photoluminescence, a decrease of the intensity of the D3 band, while G and D bands rise thus confirming a partial graphitization of the sample. In fact, despite the well-established association of the D band with defects and disorder, the appearance of this signal requires ordered graphene-like domains to be present [26].

Thermogravimetric analysis (TGA, Fig. 2b) was performed in inert atmosphere (N_2) on CNP4 in comparison with CB1 and CB2. CNP4 resulted stable up to 250 °C, indicating that the nanoparticles do not have significant amount of adsorbed species. Subsequently a continuous 40% loss of weight in the 250–700 °C range was detected. This event may be attributed to both loss of oxygenated functional groups and/or to the partial graphitization of the sample [52].

The CB2 sample showed a 15% of loss of weight, with a first loss around 150 °C likely due to the desorption of water, while CB1 owns a high stability in all range of temperatures considered, in agreement with the high degree of crystallinity.

ECNMs are intrinsically hydrophobic. However, oxygenated functionalities (-OH, -COOH, =O) may be present after synthesis or purposely inserted to increase the hydrophilicity. In fact, NPs that are intended for systemic use need to form stable aqueous suspensions. Electrostatic repulsion among particles, and consequently high ζ -potential values, either positive or negative, should be achieved in order to ensure stability and avoid agglomeration of the particles [53]. Furthermore, oxygenated functionalities provide a suitable linkage for a wide range of moieties.

Fig. 2c reports the ζ -potential values of CNP4 and reference samples suspended in ultrapure water at 25 °C as function of pH. All samples exhibit a negative zeta potential in the pH range from 2 to 10 that gradually increases with increasing of the pH of the suspension. These values indicate that the nanoparticles are surrounded by hydrophilic negatively-charged groups, likely acidic carboxylic or phenolic groups formed during the synthesis.

The presence of acidic groups was confirmed and quantified by titration using the dye thionine acetate [29,30]. It was found that a single particle of CNP4 is decorated by 4×10^4 acidic groups having a density of 3 groups/nm^2. CB1 exhibited a density of 0.96 groups/nm^2, in agreement with the ζ -potential values less negative than CNP4.

Optical properties.

The absorption spectra of CNP4 and reference spectra suspended in water were recorded in the UV–vis–NIR range (Fig. S7, SM). As expected, the carbon black samples were opaque in the whole range. CNP4 also absorb light in the whole range, however, the absorbance in the NIR region was much lower than the carbon black samples. This was expected due to the less extended sp^2 carbon framework, as shown by Raman analysis [54].

Previous studies indicate that some ECNM exhibit fluorescence [21,55,56]. In the present case, the fluorescence spectra (Fig. S8, SM) revealed obvious excitation-dependent emission spectra, which present maximum of emission in the wavelength range of 345–375 nm. The confocal microscopy analysis of the CNP4 suspension in water was also performed in order to confirm the fluorescence properties of the NPs. The nanoparticles emit in the blue light range after excitation in the 340–360 nm range (Fig. S8, SM, inset).

Photo-thermal and photodynamic properties.

PT activity under NIR laser beam irradiation was investigated in comparison with the two reference samples CB1 and CB2 by monitoring the temperature of the suspension during exposure to NIR radiation for 10 min. As shown in Fig. 3a, all the NPs produced intense heat release. Irradiation of the CNP4 suspension induced an increase of the temperature of 40 °C by respect to water in less than 3 min. The thermal effect was lower to those observed with CB1 sample, in agreement with the lower optical absorbance in the NIR region (Fig. S7, SM), but still enough to reach a temperature enough for cell death induction. Unexpectedly, a lower thermal capacity was found for CB2 by respect to CB1. Since the optical absorbance in the NIR region of CB2 was higher than CB1 (Fig. S7, SM) this result suggests that heat dissipation capacity increases with the graphitic degree of the material, thus confirming what found previously on carbon nanotubes [57].

PD properties rely on the ability of the NPs to undergo energy or electron transfer reactions to oxygen once activated by light. Two different mechanisms are known. In the first (type I reactions) superoxide radicals ($O_2^{\cdot-}$) are generated while in the second mechanism (type II) reactions singlet oxygen ($^1O_2$) is generated [58]. Superoxide radicals undergo a series of well-known reactions that lead to the generation of the highly cytotoxic hydroxyl radicals ($OH\cdot$) [59].

The ability of the carbon samples to generate ROS upon NIR radiation was studied using the EPR spectroscopy coupled with the spintrapping technique. The generation of reduced species of oxygen (hydroxyl or superoxide radicals) was monitored by using the spin trap DMPO while the probe 4-oxo-TMP was used to monitor the generation of the singlet oxygen ($^1O_2$). This probe specifically reacts with singlet oxygen generating the stable free radical 4-oxo-TEMPO that exhibits a (1:1:1) three lines spectra (aN = 15.7 G) [59]. For comparison, a commercial sample of fullerene functionalized with hydroxyl groups $C_{60}(OH)_n$, was used as positive control [60]. Following irradiation with the NIR laser beam of an aqueous suspension of CNP4, no signal was obtained using the spin trap DMPO (data not shown) while the typical spectra of 4-oxo-TEMPO was observed using the 4-oxo-TMP probe (Fig. 3b). This indicates that the material is able to transfer the absorbed energy to the ground state triplet oxygen by a type II mechanism generating singlet oxygen, while no type I mechanism was observed.

The experiments were repeated i. by fluxing with nitrogen to remove oxygen or ii. in the presence of the singlet oxygen scavenger sodium azide (Fig. S9, SM). In both cases a significant reduction of the signal was observed further confirming the generation of singlet oxygen.

From the intensity of the EPR spectra in Fig. 3b it is possible to observe that, similarly to CB1, CNP4 are able to generate singlet oxygen with and efficiency higher than fullerenol, while CB2 appears inert. In the latter case in fact, a single pick only was observed, not due to ROS but to the presence of isolated carbon-centred radical species confined in the internal structure of the material [61].

To the best of our knowledge, this is first study reporting the intrinsic ability of saccharides-derived nanoparticles to generate singlet oxygen. Albeit the structural heterogeneity of the particles hampers a detailed description of the photo-chemical processes leading to ROS generation, we undoubtedly confirm the presence of moieties able to be excited to a singlet state S1 that in turn undergo intersystem crossing to a T1 triplet state having halftime long enough to transfer energy to ground oxygen. On the other hand, the excited electrons and the correspondent positive holes of such moieties do not have a redox potential allowing the reduction of oxygen to superoxide. Oppositely to the release of heat, the generation of singlet oxygen does not appear to be correlated to the graphitic degree of the materials.

Redox activity of CNP.

ECNMs exhibit antioxidant properties due to their ability to scavenge ROS. This property has been early reported for fullerene [62], carbon nanotubes [13,63], and carbon soot [61].

The antioxidant efficiency appears related to the structural characteristics of ECNMs [56]. For example, diameter, length, composition, abundance of defects and chirality are known to modulate the scavenging activity of SWCNTs [64–68]. Defects are particularly effective in modulating the antioxidant activity since their abundance modifies the ratio between sp^2 and sp^3 hybridized carbon atoms that in turn modulate the electronic properties of the material. In fact, the scavenging may occur through different pathways, like electron exchange between the particle and the radical specie, addition of the radical on the carbon backbone [61] and, furthermore, by hydrogen donation to the free radical species by surface functionalities [69].

The scavenging activity of carbon nanoparticles toward the most aggressive ROS, hydroxyl radicals (HO·), was tested by means of EPR spectroscopy coupled with spin trapping technique. Hydroxyl radicals were generated by the Fenton reaction as described in the method section. The high amount of radicals generated in this condition is proved by the intense (1:2:2:1) four-line EPR signal recorded, correspondent to the DMPO/HO· adduct (aN=aH= 14.6 G) (Fig. 4a). When the reaction was performed in the presence of the nanoparticles, the signal was completely suppressed in the case of CB1 and CB2, while for CNP4 the EPR signal decreased, suggesting a scavenging capability lower than the reference samples. The higher activity observed for the carbon black samples might be due to an abundance of crystalline patches higher by respect to CNP4. This suggests a mechanism involving the addition of free radicals to the carbon backbone or, alternatively, an electron transfer process. Conversely, a mechanism due to hydrogen donation from the functional groups exposed to the surface to the hydroxyl radicals may be excluded since CNP4, exhibit abundance of surface functionalities higher than CB1.

Liu et al. [14] previously reported the ability of some ECNMs to oxidize glutathione, one of the main antioxidant molecules of cells. In cells, this property may result in a pro-oxidant effect. The oxidative potency of CNP4 was tested in comparison with two reference samples by monitoring the glutathione depletion capacity. Fig. 4b shows the degree of oxidation of GSH after 2 h of interaction with CNP4 or with the reference samples, quantified by the Ellman's reagent. The effects of CNP4 and CB2 on GSH are comparable, while the depletion caused by CB1 was lower. According to Liu et al., [14] a correlation between the exposed surface area and the amount of

GSH consumed exists. In the present case, when compared at equal surface area (Fig. 4b), the two carbon black samples exhibit a similar specific reactivity, thus confirming the role of surface area previously reported by Liu et al. However, in the case of CNP4 a higher reactivity was observed. The UV–Vis spectra recorded on the supernatant after incubation of the samples with GSH were also recorded (Fig. S10, SM). A spectrum having a maximum at around 300 nm likely due to generation of an oxidized form of glutathione was observed for all samples, demonstrating that the decrease in GSH concentration was due to its oxidation and not to an adsorption of the molecules at the NP surfaces.

The peculiar reactivity of CNP4 might be attributed to a different abundance of active sites that Liu et al. suggested to be superoxide radicals adsorbed at the surface. Note that the capacity of CNP4 to consume glutathione (2.26 µmol/mg) was much higher when compared with the amount of hydroxyl radicals scavenged (0.00475 µmol/mg) suggesting the prevalence of the antioxidant properties.

Characterization of nanoparticles in cell media.

The size distribution and stability of CNP4 in the cell media was evaluated by DLS, at different time incubation correspondent to those used in cellular tests (0, 24 and 48 h). The analyses (Fig. S11, SM) showed one single population of particles having mean hydrodynamic diameter around 200 nm, compatible with the presence of monodisperse particles surrounded with a protein corona. No agglomeration or change in mean hydrodynamic diameter was observed during the 48 h of incubation.

Cytotoxicity toward RAW 264.7 and uptake.

CNP were firstly tested for their ability to induce cytotoxicity, measured as leakage of intracellular LDH into the extracellular medium. RAW 264.7 macrophages were incubated for 24 or 48 h with the NPs at a concentration range of 10–320 µg/ml (Fig. 5a). A sample of pyrogenic silica was used as positive control [70]. CNP4 do not elicit any cytotoxic effect on macrophages in a wide range of concentrations. A significant cytotoxic effect was observed only after 48 h of

exposure with CNPs at the very high concentrations of 160 μg/ml (Fig. 5a). On the other hand, in these conditions, an effect due to overload is likely.

TEM analysis was performed on RAW 264.7 incubated in the presence of CNP4 (Fig. 5b). Unexposed cells (negative control) showed normal morphology without specific ultrastructure alterations. Nuclei are well defined and all the organelles visible. Cells exposed at 40 μg/ml and 160 μg/ml of CNP4 for 24 and 48 h respectively, show groups of single particles inside endo/phagocytosis organelles (endosomes) with an increased dose and time dependent uptake. No sign of lysis of the phagolysosome membranes was observed. These results exclude that the observed low toxicity was a consequence of the absence of uptake of the particles by macrophages. The mechanism of uptake is known to depend upon the size and surface charge of nanoparticles [71]. In the present case, since CNP4 are not conjugated with targeting agents, an aspecific endocytosis is expected. In this case, the small size and the negative surface of CNP4 should favour their cellular uptake. In fact, although still controversial, there are evidences that anionic nanoparticles are more internalized than cationic ones due to the favourable electrostatic interactions between the surface of the particles and the cell plasma-membrane [72,73].

Effect of CNP4 on the redox homeostasis of macrophages.

CNPs to modulate the redox homeostasis in macrophages was evaluated by measuring the generation of ROS or NO on non-activated or lipopolysaccharide-activated macrophages following incubation with the NPs at non-cytotoxic concentrations (40–80 μg/ml) (Fig. 6a,b). The NPs did not induce ROS or NO production by macrophages under basal conditions. On the contrary, when cells activated with 1 μg/ml LPS were incubated with CNP4, a clear, dose dependent, inhibition of ROS and NO generation was observed, indicating that an antioxidant behaviour of NPs prevails in activated macrophages. To get insight onto the molecular mechanism of this effect, the amount of intracellular reduced glutathione was also measured (Fig. 6c): we did not observe any change in reduced intracellular GSH, suggesting that the GSH consumed by the NPs, as shown by cell-free tests, is efficiently restored by the glutathione reductase system of cells. The predominant antioxidant effect may be therefore attributed to the scavenging ability of the nanoparticles toward hydroxyl radicals.

Since ROS and NO are typical signs or macrophage activation during inflammatory diseases (e.g. atherosclerosis, vasculitis, rheumatoid arthritis) [74], our results suggest a potential use of CNPs in mitigating the damages induced by activated macrophages on neighbour cells.

Furthermore, the low toxicity and the antioxidant effect toward macrophages suggest a possible safe use of these nanoparticles in nanomedicine. On the other hand, the antioxidant capability may mitigate the oxidative burst typical of activated cells during photo-thermal or photodynamic treatments. Further studies are in progress to investigate this latter aspect.

Effect of CNP4 on the cytokines production of macrophages.

Cytokines production is a paramount parameter of macrophages activation. To investigate how CNP4 affect this issue, we measured the levels of TNF-α, chosen as a paradigmatic pro-inflammatory cytokine, and IL-10, chosen as a paradigmatic immune-suppressive cytokine, in RAW 264.7 cells, treated with CNP4 at 40 and 80 µg/ml for 24 h, two concentrations that were not cytotoxic (Fig. 5a), did not alter intracellular ROS and GSH, nor production of nitrite (Fig. 6), either in unstimulated macrophages or in LPS-stimulated (i.e. activated) macrophages. As shown in Fig. 7, both concentrations increased the production of TNF-α in resting macrophages. On the other hand, when LPS was added to mimic the typical macrophage activation occurring in inflammatory situations [75] (e.g. cardiovascular diseases, bacterial infections, cancers) CNP4 did not further increase TNF-α, meaning that they do not amplify the TNF-α-mediated inflammation. Moreover, CNP4 did not significantly alter IL-10 production, neither in basal conditions nor upon LPS stimulation, a strong inducer of IL-10 production in macrophages [76]. In the oncological setting, a chronic inflammation sustained by activated macrophages favours tumour progression. Such prolonged activation, however, paradoxically leads to immune-system exhaustion, inducing an immune-suppressive status that further promotes tumour growth [77]. One of the most common signs is the production of IL-10 by macrophages, that become pro-tumourigenic [77]. Overall, this experimental set suggests that CNP4 did not exacerbate the production of TNF-α nor IL-10 in activated macrophages. Since CNP4 prevent the undesired production of cytokines that amplify inflammation and/or shift the micro-environment from inflammation to immune-suppression, our data reinforce the assumption that CNP4 are promising tools for those conditions where an excessive activation of macrophages is dangerous, such as cardiovascular and chronic inflammatory diseases potentially leading to tumourigenesis.

Conclusions

In conclusion, CNP4 exhibit both pro- and anti-oxidant capabilities in cell-free system. However, in macrophages the antioxidant effect prevails suggesting a possible protective effect from the oxidative/nitrosative damage produced by activated macrophages. Following NIR activation CNP exhibit PT and PD properties. Interestingly, all these properties appear to be modulated by the bulk structure of carbon NPs, thus suggesting a possible optimization of these functional properties. We believe that the present findings contribute to the advancement in a safe use of elemental carbon NPs in nanomedicine. Furthermore, they suggest a possible use in all those diseases where an improper macrophage activation is undesirable, such as cardiovascular and chronic inflammatory diseases.

Conflicts of interest

There are no conflicts to declare.

Acknowledgements

a)

| sample	precursor (g) in 50 ml H$_2$O	surfactant (mg)	time (h)	temp (°C)
CNP1	8	15	8	190
CNP2	4	15	8	190
CNP3	2	15	8	190
CNP4	2	15	3	190

b)
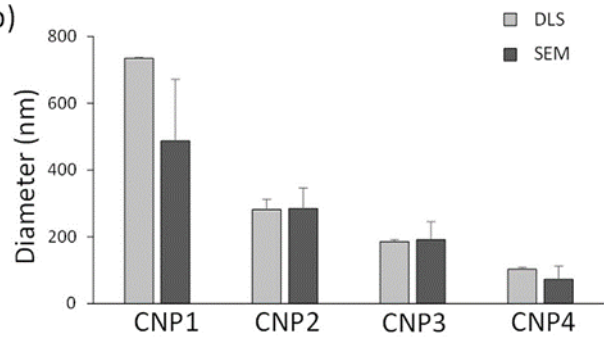
c)
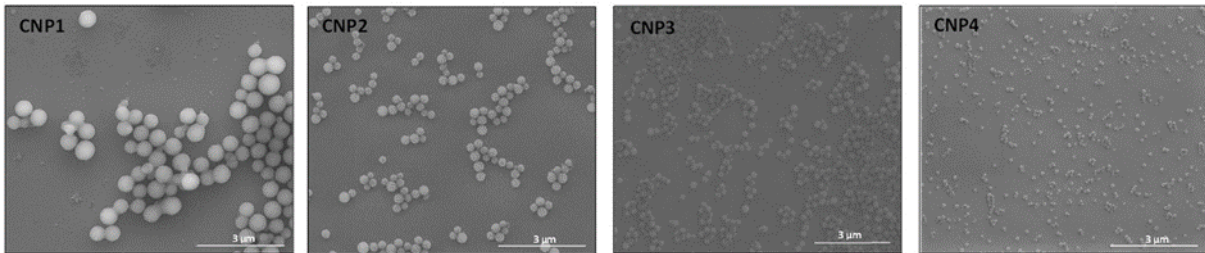
Figure 1. a) Summary of the parameters used in the synthesis of the CNPs; b) Comparison between hydrothermal diameter obtained by Dynamic light scattering (number distribution) and geometric diameter obtained by SEM imaging of the CNPs suspended in water. c) SEM images of different preparations of CNPs.
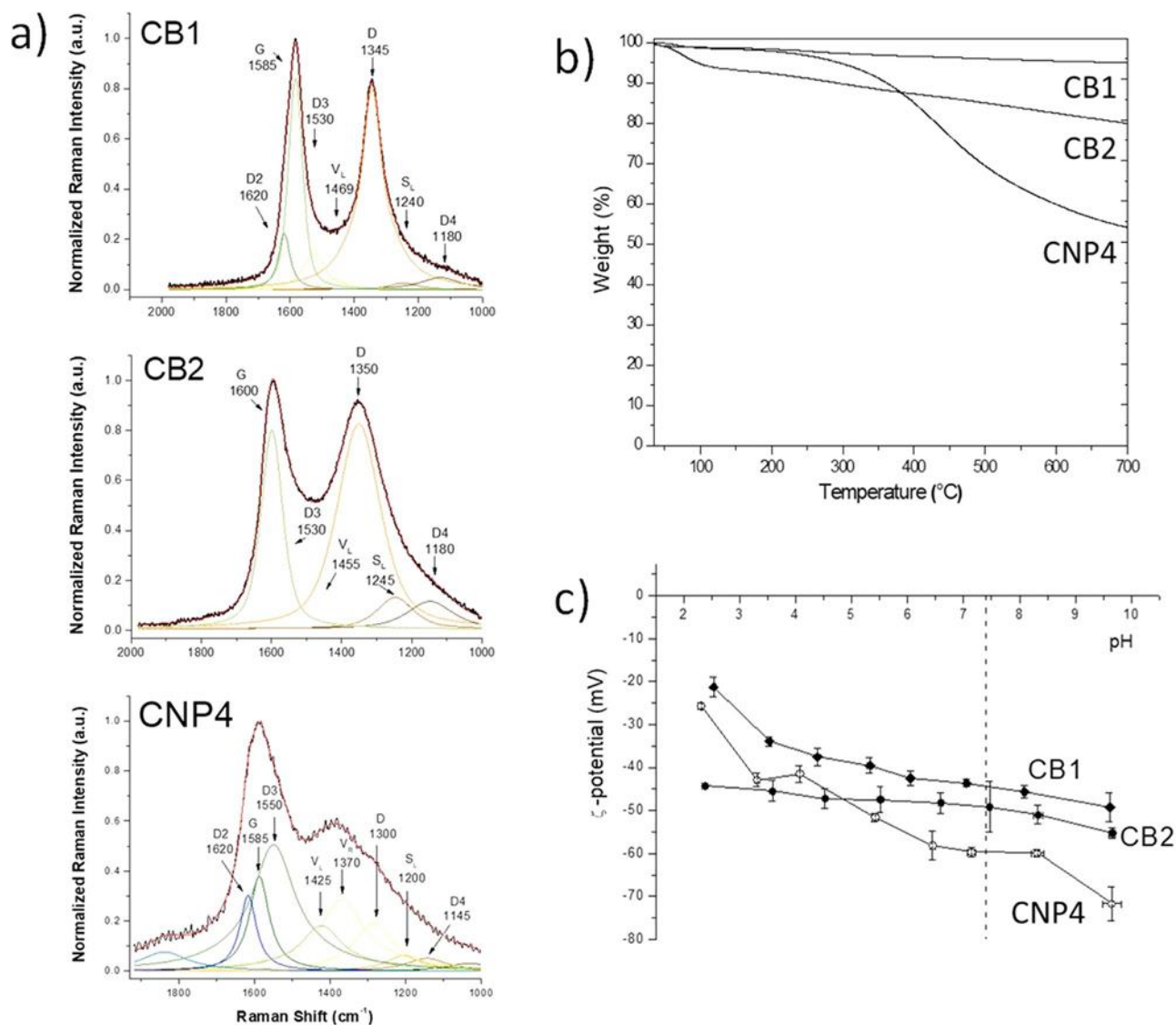
Figure 2. a) Raman spectra and deconvolution patterns of CNP4 and carbon black samples. b) TGA thermograms. % of weight loss recorded under N_2 (TGA heating ramp 15 °C/min, N_2 flow rate 35 ml/min); c) Zeta potential versus pH curves for CNP4 and reference samples suspended in water. The curves are relative to CNP4 (open circles), CB1 (squares) and CB2 (circles).
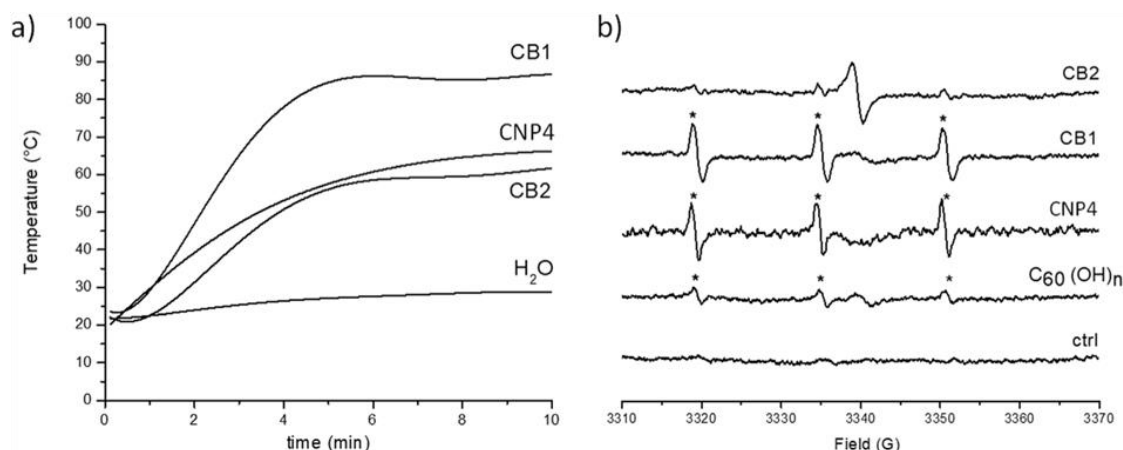
Figure 3. a) Photothermal activity. Temperature change curves of CNP4, CB1 and CB2 suspension during NIR laser irradiation; b) Singlet oxygen generation. EPR spectra generated after NIR laser irradiation of a suspension of the samples (2 mg/ml) in the presence of TMP (50.5 mM). The three lines signal correspondent to the 4-oxo-TEMPO species is indicated by asterisks.
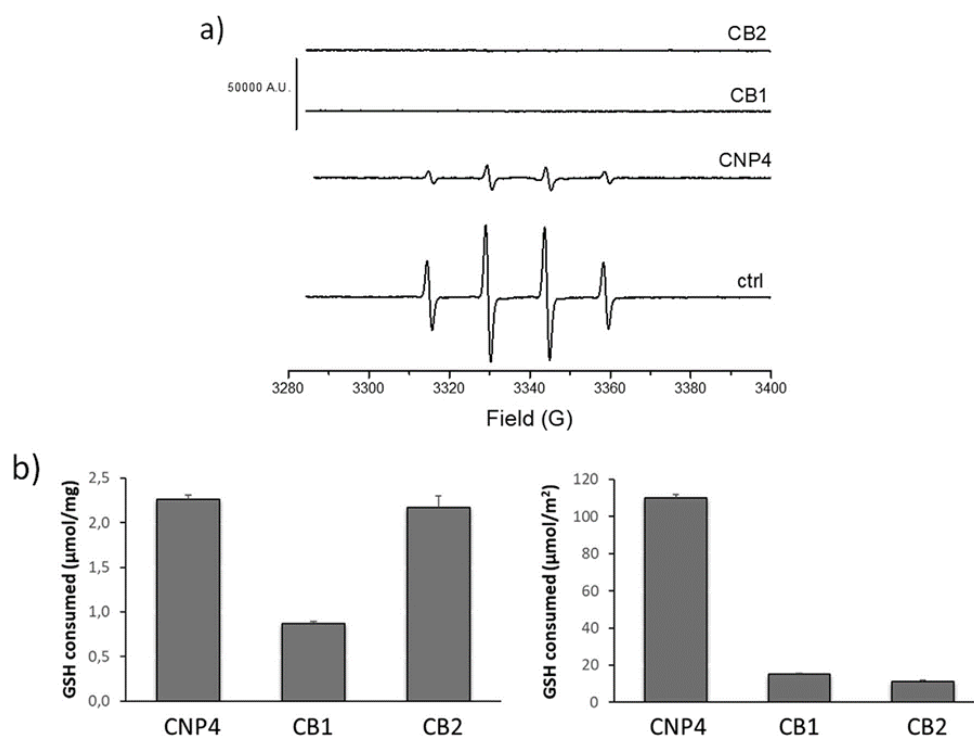

Figure 4. a) Scavenging activity toward hydroxyl radicals. EPR spectra obtained in a buffered solution containing 50 mM DMPO, 1.7 mM $FeSO_4$, 32 mM H_2O_2 (control) and in the same solution in the presence of 2 mg/ml of the CNP4 or reference samples; b) Amount of glutathione consumed following the interaction with CNP4, CB1, CB2 expressed as a function of mass (right) and as a function of surface area (left).
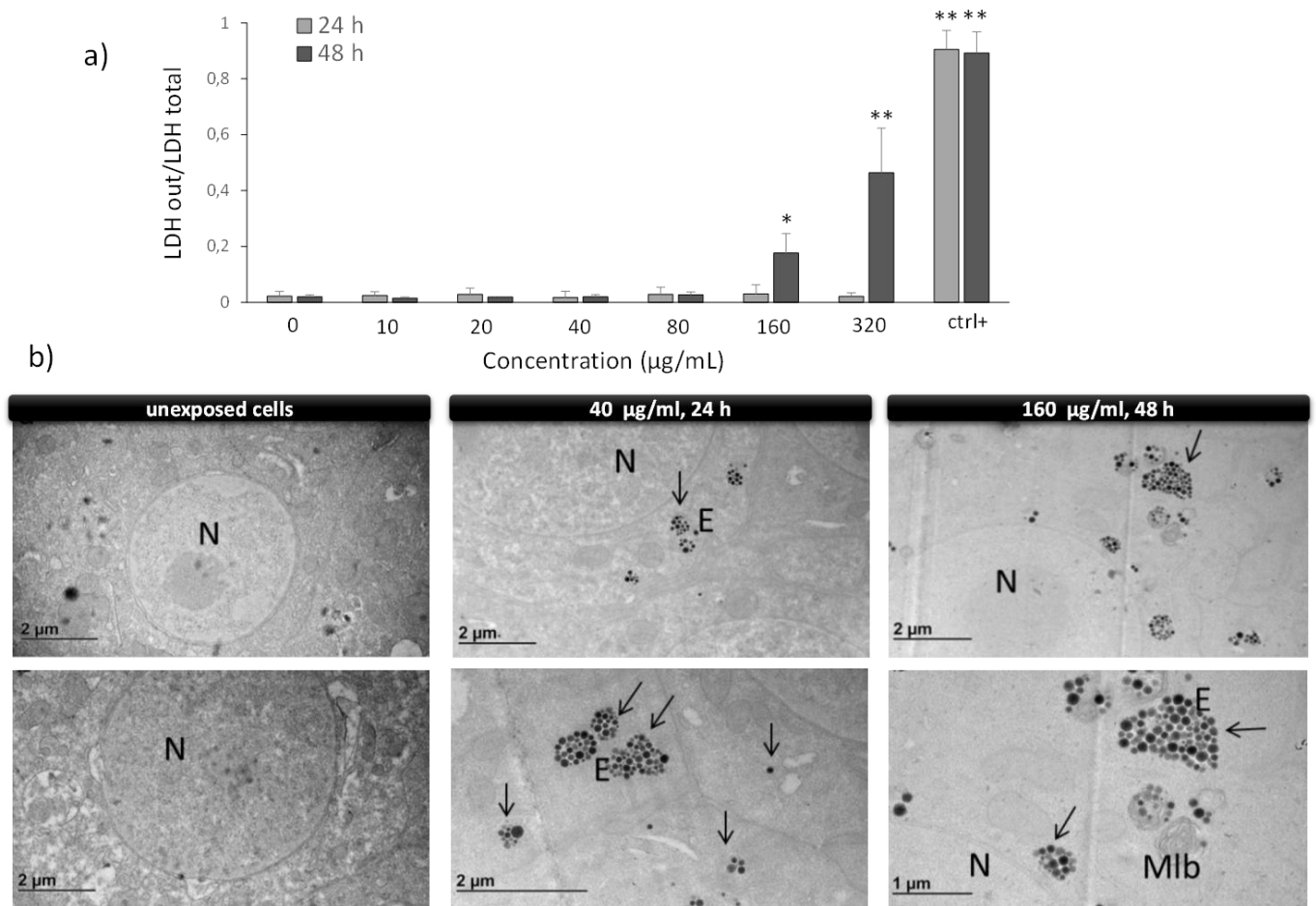
Figure 5. a) Cytotoxicity of CNP4 toward macrophages: LDH leakage following exposure to CNP4 for 24 or 48h at different doses. crl- is without the nanoparticles; a sample of amorphous silica has been used as positive control. Vs ctrl (0 µg/ml) *p < 0,05, ** p<0.01; b) internalization of CNP4 in macrophages. The arrows indicate the nanoparticles; (N) nucleus; (Mlb) multi lamellar bodies; (E) endosomes.
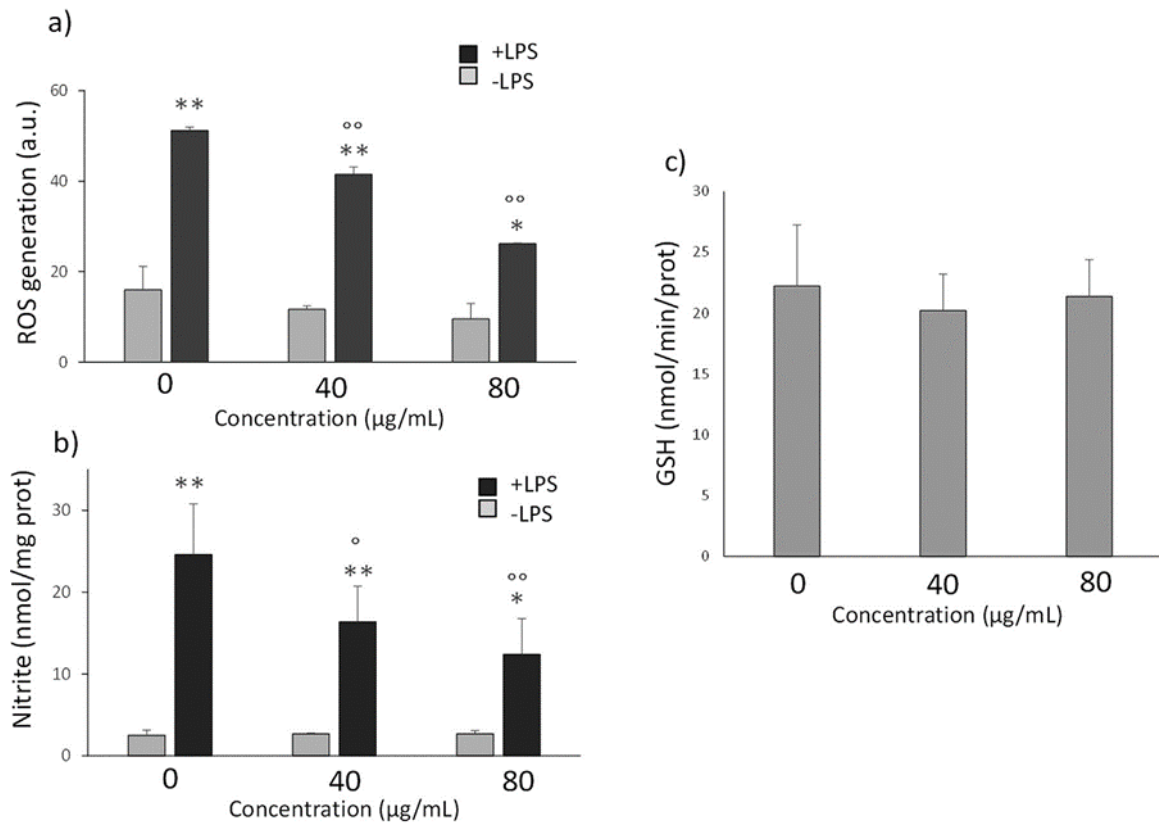
Figure 6. a) ROS generation by non-activated and LPS- activated macrophages exposed to CNP4 for 24 h at non-cytotoxic doses. b) NO generation by non-activated and LPS- activated macrophages exposed to CNP4 for 24 h at non-cytotoxic doses. c) intracellular reduced glutathione in macrophages exposed to CNP4 for 24 h at non-cytotoxic doses. Vs ctrl (0 µg/ml): ** $p<0.01$; * $p<0.05$; vs control + LPS: °° $p<0.01$; ° $p<0.05$.
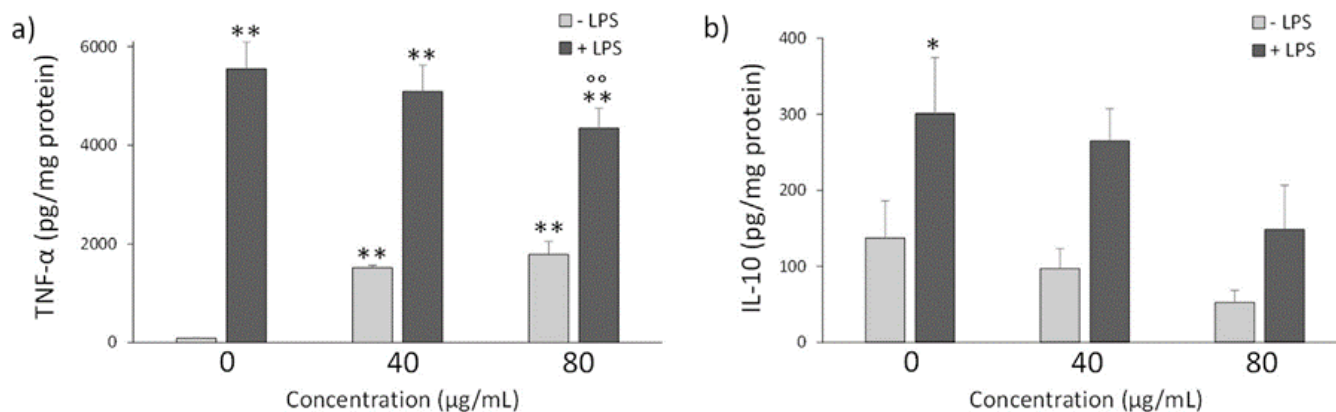
Figure 7. a) TNF-α production by non-activated and LPS- activated macrophages exposed to CNP4 for 24 h at non-cytotoxic doses. b) IL-10 production by non-activated and LPS- activated macrophages exposed to CNP4 for 24 h at non-cytotoxic doses. Vs ctrl (0 μg/ml): ** p<0.01; * p<0.05; vs control + LPS: °° p<0.01; ° p<0.05.

References

[1] R.H. Baughman, A.A. Zakhidov, W.A. de Heer, Carbon nanotubes-the route toward applications, Science 297 (2002) 787–792, https://doi.org/10.1126/science. 1060928.

[2] A.K. Geim, Graphene: status and prospects, Science 324 (2009) 1530–1534, https://doi.org/10.1126/science.1158877.

[3] K. Albert, H. Hsin-Yun, Carbon-based materials for photo-triggered theranostic applications, Molecules 21 (2016) E1585, https://doi.org/10.3390/ molecules21111585.

[4] S. Banerjee, T. Hemraj-Benny, S.S. Wong, Covalent surface chemistry of single-walled carbon nanotubes, Adv. Mater. 17 (2005) 17–19, https://doi.org/10.1002/ adma.200401340.

[5] D. Tasis, N. Tagmatarchis, A. Bianco, M. Prato, Chemistry of carbon nanotubes, Chem. Rev. 106 (2006) 1105–1136, https://doi.org/10.1021/cr050569o.

[6] G. Obaid, M. Broekgaarden, A. Bulin, H. Huang, J. Kuriakose, J. Liu, H. Tayyaba, Photonanomedicine: a convergence of photodynamic therapy and nanotechnology, Nanoscale 8 (2016) 12471–12503, https://doi.org/10.1039/C5NR08691D.

[7] C.M. Courtney, S.M. Goodman, J.A. McDaniel, N.E. Madinger, A. Chatterjee, P. Nagpal, Photoexcited quantum dots for killing multidrug-resistant bacteria, Nat. Mater. 15 (2016) 529–534, https://doi.org/10.1038/nmat4542.

[8] P. Zhang, C. Hu, W. Ran, J. Meng, Q. Yin, Y. Li, Recent progress in light-triggered nanotheranostics for cancer treatment, Theranostics 6 (2016) 948–968, https://doi. org/10.7150/thno.15217.

[9] J. Miller, Photodynamic Therapy: the sensitization of cancer cells to light, J. Chem. Educ. 76 (1999) 592–594, https://doi.org/10.1021/ed076p592.

[10]   Z. Li, C. Wang, L. Cheng, H. Gong, S. Yin, Q. Gong, Y. Li, Z. Liu, PEG-functionalized iron oxide nanoclusters loaded with chlorin e6 for targeted, NIR light induced, photodynamic therapy, Biomaterials 34 (2013) 9160–9170, https://doi.org/10. 1016/j.biomaterials.2013.08.041.

[11]   H. Kim, K. Chung, S. Lee, D.H. Kim, H. Lee, Near-infrared light-responsive nanomaterials for cancer theranostics, WIREs Nanomed. Nanobiotechnol. 8 (2016) 23–45, https://doi.org/10.1002/wnan.1347.

[12]   M. Ghiazza, G. Vietti, I. Fenoglio, Carbon nanotubes: properties, applications, and toxicity, in: J. Njuguna, K. Pielichowski, H. Zhu (Eds.), Composites Science and Engineering No. 49, Woodhead Publishing, U.K, 2014, pp. 147–174, , https://doi. org/10.1533/9780857096678.3.147.

[13]   I. Fenoglio, M. Tomatis, D. Lison, J. Muller, A. Fonseca, J.B. Nagy, B. Fubini, Reactivity of carbon nanotubes: free radical generation or scavenging activity? Free
Radic. Biol. Med. 40 (2006) 1227–1233, https://doi.org/10.1016/j.freeradbiomed. 2005.11.010.

[14]   X. Liu, S. Sen, J. Liu, I. Kulaots, D. Geohegan, A. Kane, Alex A. Puretzky, C.M. Rouleau, K.L. More, G.T.R. Palmore, R.H. Hurt, Antioxidant deactivation on graphenic nanocarbon surfaces, Small 7 (2011) 2775–2785, https://doi.org/10. 1002/smll.201100651.

[15]   S. Galadaria, A. Rahman, S. Pallichankandy, F. Thayyullathil, Reactive oxygen species and cancer paradox: to promote or to suppress? Free Rad. Biol. Med. 104 (2017) 144–164, https://doi.org/10.1016/j.freeradbiomed.2017.01.004.

[16]   Z. Markovic, V. Trajcovic, Biomedical potential of the reactive oxygen species generation and quenching by fullerenes (C_{60}), Biomaterials 29 (2008) 3561–3573, https://doi.org/10.1016/j.biomaterials.2008.05.005.

[17]   C.-Y. Chen, C.T. Jafvert, The role of surface functionalization in the solar lightinduced production of reactive oxygen species by single-walled carbon nanotubes in water, Carbon 49 (2011) 5099–5106, https://doi.org/10.1016/j.carbon.2011.07. 029.

[18]   R. Demir-Cakan, N. Baccile, M. Antonietti, M. Titirici, Carboxylate-rich carbonaceous materials via one-step hydrothermal carbonization of glucose in the presence of acrylic acid, Chem. Mater. 21 (2009) 484–490, https://doi.org/10.1021/ cm802141h.

[19]   Z. Yi, Y. Liang, X. Lei, C. Wang, J. Sun, Low-temperature synthesis of nanosized disordered carbon spheres as an anode material for lithium ion batteries, Mater.
Lett. 61 (2007) 4199–4203, https://doi.org/10.1016/j.matlet.2007.01.054.

[20]   M. Ajmal, U. Yunus, A. Matin, N.U. Haq, Synthesis, characterization and in vitro evaluation of methotrexate conjugated fluorescent carbon nanoparticles as drug delivery system for human lung cancer targeting, J. Photochem. Photobiol. B 153 (2015) 111–120, https://doi.org/10.1016/j.jphotobiol.2015.09.006.

[21] N. Li, T. Li, C. Hu, X. Lei, Y. Zuo, H. Han, Targeted near-infrared fluorescent turn-on nanoprobe for activatable imaging and effective phototherapy of cancer cells, ACS Appl. Mater. Interfaces 8 (2016) 15013–15023, https://doi.org/10.1021/acsami. 5b02037.

[22] Z. Miao, H. Wang, H. Yang, Z. Li, L. Zhen, C. Xu, Glucose-derived carbonaceous nanospheres for photoacoustic imaging and photothermal therapy, ACS Appl. Mater. Interfaces 8 (2016) 15904–15910, https://doi.org/10.1021/acsami. 6b03652.

[23] B.R. Selvi, D. Jagadeesan, B.S. Suma, G. Nagashankar, M. Arif, K. Balasubramanyam, M. Eswaramoorthy, Tapas K. Kundu, Intrinsically fluorescent carbon nanospheres as a nuclear targeting vector: delivery of membrane-impermeable molecule to modulate gene expression in vivo, Nano Lett. 8 (2008) 3182–3188, https://doi.org/10.1021/nl801503m.

[24] D. Wei, R. Dave, R. Pfeffer, Mixing and characterization of nanosized powders: an assessment of different techniques, J. Nanopart. Res. 4 (2002) 21–41, https://doi. org/10.1023/A:1020184524538.

[25] F. Tuinstra, J.L. Koenig, Raman spectrum of graphite, J. Chem. Phys. 53 (1970) 1126–1130, https://doi.org/10.1063/1.1674108.

[26] A.C. Ferrari, J. Robertson, Interpretation of Raman spectra of disordered and amorphous carbon, Phys. Rev. B 61 (2000) 14095–14107, https://doi.org/10. 1103/PhysRevB.61.14095.

[27] A. Sadezky, H. Muckenhuber, H. Grothe, R. Niessner, U. Pöschl, Raman microspectroscopy of soot and related carbonaceous materials: spectral analysis and structural information, Carbon 43 (2005) 1731–1742, https://doi.org/10.1016/j. carbon.2005.02.018.

[28] X. Li, J.I. Hayashi, C.Z. Li, FT-Raman spectroscopic study of the evolution of char structure during the pyrolysis of a Victorian brown coal, Fuel 85 (2006) 1700–1707, https://doi.org/10.1016/j.fuel.2006.03.008.

[29] A. Pietroiusti, M. Massimiani, I. Fenoglio, M. Colonna, F. Valentini, G. Palleschi, A. Camaioni, A. Magrini, G. Siracusa, A. Bergamaschi, A. Sgambato, L. Campagnolo, Low doses of pristine and oxidized single-wall carbon nanotubes affect mammalian embryonic development, ACS Nano 5 (2011) 4624–4633, https://doi.org/10.1021/ nn200372g.

[30] S. Visentin, N. Barbero, S. Musso, V. Mussi, C. Biale, R. Ploeger, G. Viscardi, A sensitive and practical fluorimetric test for CNT acidic site determination, Chem. Commun. 46 (2010) 1443–1455, https://doi.org/10.1039/B920311G.

[31] B. Tian, C. Wang, S. Zhang, L. Feng, Z. Liu, Photothermally enhanced photodynamic therapy delivered by nano-graphene oxide, ACS Nano 5 (2011) 7000–7009, https:// doi.org/10.1021/nn201560b.

[32] R. Gassino, I. Kokalari, A. Vallan, I. Fenoglio, Guido Perrone, A compact diode laser based all-fiber delivery system for PDT+PTT with integrated temperature sensing capabilities, in: D.H. Kessel, T. Hasan (Eds.), Proc. SPIE No. 10047, Int. Soc. Optical Engineering, USA, 2017, , https://doi.org/10.1117/12.2254796.

[33]   F. Tietze, Enzymic method for quantitative determination of nanogram amounts of total and oxidized glutathione: applications to mammalian blood and other tissues, Anal. Biochem. 27 (1969) 502–522, https://doi.org/10.1016/0003-2697(69) 90064-5.

[34]   M. Polimeni, E. Gazzano, M. Ghiazza, I. Fenoglio, A. Bosia, B. Fubini, D. Ghigo, Quartz inhibits glucose 6-phosphate dehydrogenase in murine alveolar macrophages, Chem. Res. Toxicol. 21 (2008) 888–894, https://doi.org/10.1021/ tx7003213.

[35]   A. Kroll, M.H. Pillukat, D. Hahn, J. Schnekenburger, Interference of engineered nanoparticles with in vitro toxicity assays, Arch. Toxicol. 86 (2012) 1123–1236, https://doi.org/10.1007/s00204-012-0837-z.

[36]   G.R. Gulino, M. Polimeni, M. Prato, E. Gazzano, J. Kopecka, S. Colombatto, D. Ghigo, E. Aldieri, Effects of chrysotile exposure in human bronchial epithelial cells: insights into the pathogenic mechanisms of asbestos-related diseases, Environ.
Health Perspect. 124 (2016) 776–784, https://doi.org/10.1289/ehp.1409627.

[37]   Q. Wang, H. Li, L. Chen, X. Huang, Monodispersed hard carbon spherules with uniform nanopores, Carbon 39 (2001) 2211–2214, https://doi.org/10.1016/S00086223(01)00040-9.

[38]   Y. Gong, H. Wang, Z. Wei, L. Xie, Y. Wang, An efficient way to introduce hierarchical structure into biomass-based hydrothermal carbonaceous materials, ACS Sustain. Chem. Eng. 2 (2014) 2435–2441, https://doi.org/10.1021/sc500447j.

[39]   P. Zhang, Z. Qiao, S. Dai, Recent advances in carbon nanospheres: synthetic routes and applications, Chem. Commun. 51 (2015) 9246–9256, https://doi.org/10.1039/ C5CC01759A.

[40]   Y. Gong, L. Xie, H. Li, Y. Wang, Sustainable and scalable production of monodisperse and highly uniform colloidal carbonaceous spheres using sodium polyacrylate as the dispersant, Chem. Commun. 50 (2014) 12633–12636, https://doi. org/10.1039/C4CC04998E.

[41]   F. Danhier, N. Lecouturier, B. Vroman, C. Jérôme, J. Marchand- Brynaert, O. Feron, V. Préat, Paclitaxel-loaded PEGylated PLGA-based nanoparticles: in vitro and in vivo evaluation, J. Control Release 133 (2009) 11–17, https://doi.org/10.1016/j. jconrel.2008.09.086.

[42]   J. Zhao, M.H. Stenzel, Entry of nanoparticles into cells: the importance of nanoparticle properties, Polym. Chem. 9 (2018) 259–272, https://doi.org/10.1039/ C7PY01603D.

[43]   A. Jorio, G. Dresselhaus, M.S. Dresselhaus, Raman Spectroscopy in Nanoscience and Nanometrology: Carbon Nanotubes, Nanographite and Graphene, Wiley-VCH, Hoboken, NJ, 2010.

[44]   H.M. Heise, R. Kuckuk, A.K. Ojha, A. Srivastava, V. Srivastava, B.P. Asthana, Characterisation of carbonaceous materials using Raman spectroscopy: a comparison of carbon nanotube filters, single- and multi-walled nanotubes, graphitised porous carbon and graphite, J. Raman Spectrosc. 40 (2009) 344–353, https://doi. org/10.1002/jrs.2120.

[45]   A. Cuesta, P. Dhamelincourt, J. Laureyns, A. Martinezalonso, J.M.D. Tascon, Raman microprobe studies on carbon materials, Carbon 32 (1994) 1523–1532, https://doi. org/10.1016/0008-6223(94)90148-1.

[46]   A. Ferrari, Raman spectroscopy of graphene and graphite: disorder, electron–phonon coupling, doping and nonadiabatic effects, Solid State Commun. 143 (2007) 47–57, https://doi.org/10.1016/j.ssc.2007.03.052.

[47] J. Schwan, S. Ulrich, V. Batori, H. Ehrhardt, S.R.P. Silva, Raman spectroscopy on amorphous carbon films, J. Appl. Phys. 80 (1996) 440–447, https://doi.org/10. 1063/1.362745.

[48] J. McDonald-Wharry, M. Manley-Harris, K. Pickering, Carbonisation of biomassderived chars and the thermal reduction of a graphene oxide sample studied using Raman spectroscopy, Carbon 59 (2013) 383–405 (https://doi.org/ j.carbon.2013.03.033).

[49] M. Wang, D.G. Roberts, M.A. Kochanek, D.J. Harris, L. Chang, C. Li, Raman spectroscopic investigations into links between intrinsic reactivity and char chemical structure, Energy Fuels 28 (2014) 285–290, https://doi.org/10.1021/ef401281h.

[50] M. Sevilla, A.B. Fuertes, Chemical and structural properties of carbonaceous products obtained by hydrothermal carbonization of saccharides, Chem. Eur. J. 15 (2009) 4195–4203, https://doi.org/10.1002/chem.200802097.

[51] O. Frank, G. Tsoukleri, J. Parthenios, K. Papagelis, I. Riaz, R. Jalil, K.S. Novoselov, C. Galiotis, Compression behavior of single-layer graphenes, ACS Nano 4 (2010) 3131–3138, https://doi.org/10.1021/nn100454w.

[52] L. Yu, C. Falco, J. Weber, R.J. White, J.Y. Howe, M. Titirici, Carbohydrate-derived hydrothermal carbons: a thorough characterization study, Langmuir 28 (2012) 12373–12383, https://doi.org/10.1021/la3024277.

[53] I. Bala, S. Hariharan, R. Kumar, PLGA nanoparticles in drug delivery: the state of the art, Crit. Rev. Ther. Drug Carr. Syst. 21 (2004) 387–422, https://doi.org/10. 1615/CritRevTherDrugCarrierSyst.v21.i5.20.

[54] A.M. Schrand, B.M. Stacy, S. Payne, L. Dosser, S.M. Hussain, Fundamental examination of nanoparticle heating kinetics upon near infrared (NIR) irradiation, ACS Appl. Mater. Interfaces 3 (2011) 3971–3980, https://doi.org/10.1021/ am2008536.

[55] M. Sevilla, A.B. Fuertes, D.C. Rezan, M.M. Titirici, M.-M. Titirici (Ed.), Sustainable Carbon Materials from Hydrothermal Processes, John Wiley & Sons, Ltd, Oxford, UK, 2013, pp. 213–294, , https://doi.org/10.1002/9781118622179.

[56] Y. Sun, B. Zhou, Y. Lin, W. Wang, K.A.S. Fernando, P. Pathak, M.J. Meziani, B.A. Harruff, X. Wang, H. Wang, P.G. Luo, H. Yang, M.E. Kose, B. Chen, L.M. Veca, S. Xie, Quantum-sized carbon dots for bright and colorful photoluminescence, J. Am. Chem. Soc. 128 (2006) 7756–7757, https://doi.org/10.1021/ja062677d.

[57] R. Singh, S.V. Torti, Carbon nanotubes in hyperthermia therapy, Adv. Drug Deliv. Rev. 65 (2013) 2045–2060, https://doi.org/10.1016/j.addr.2013.08.001.

[58] M. Ochsner, J. Photophysical and photobiological processes in the photodynamic therapy of tumours, J. Photochem. Photobiol. B: Biol. 39 (1997) 1–18, https://doi. org/10.1016/S1011-1344(96)07428-3.

[59] M. Ghiazza, E. Alloa, S. Oliaro-Bosso, F. Viola, S. Livraghi, D. Rembges, R. Capomaccio, F.O. Rossi, J. Ponti, I. Fenoglio, Inhibition of the ROS-mediated cytotoxicity and genotoxicity of nano-TiO2 toward human keratinocyte cells by iron doping, J. Nanopart. Res. 16 (2014) 2263–2280, https://doi.org/10.1007/s11051014-2263-z.

[60] B. Vileno, P.R. Marcoux, M. Lekka, A. Sienkiewicz, T. Fehér, L. Forró, Spectroscopic and photophysical properties of a highly derivatized C_{60} fullerol, Adv. Funct. Mater. 16 (2006) 120–128, https://doi.org/10.1002/adfm.200500425.

[61] E. Carella, M. Ghiazza, M. Alfè, E. Gazzano, D. Ghigo, V. Gargiulo, A. Ciajolo, B. Fubini, I. Fenoglio, Graphenic nanoparticles from combustion sources scavenge hydroxyl radicals depending upon their structure, BioNanoSci 3 (2013) 112–122, https://doi.org/10.1007/s12668-013-0077-6.

[62] L.L. Dugan, D.M. Turetsky, C. Du, D. Lobner, M. Wheeler, C.R. Almli, C.K.F. Shen, T. Luh, D.W. Choi, T. Lin, Carboxyfullerenes as neuroprotective agents, Proc. Natl. Acad. Sci. USA 94 (1997) 9434–9439, https://doi.org/10.1073/pnas.94.17.9434.

[63] S. Tsuruoka, H. Matsumoto, K. Koyama, E. Akiba, T. Yanagisawa, F.R. Cassee, N. Saito, Y. Usui, S. Kobayashi, D.W. Porter, V. Castranova, M. Endo, Radical scavenging reaction kinetics with multiwalled carbon nanotubes, Carbon 83 (2015) 232–239, https://doi.org/10.1016/j.carbon.2014.10.009.

[64] I. Fenoglio, G. Greco, M. Tomatis, J. Muller, E. Raymundo-Piñero, F. Béguin, A. Fonseca, J.B. Nagy, D. Lison, B. Fubini, Structural defects play a major role in the acute lung toxicity of multiwall carbon nanotubes: physicochemical aspects, Chem. Res. Toxicol. 21 (2008) 1690–1697, https://doi.org/10.1021/tx800100s.

[65] A. Galano, Carbon nanotubes: promising agents against free radicals, Nanoscale 2 (2010) 373–380, https://doi.org/10.1039/b9nr00364a.

[66] A. Galano, Influence of diameter, length, and chirality of single-walled carbon nanotubes on their free radical scavenging capability, J. Phys. Chem. C 113 (2009) 18487–18491, https://doi.org/10.1021/jp904646q.

[67] A. Martinez, A. Galano, Free radical scavenging activity of ultrashort single-walled carbon nanotubes with different structures through electron transfer reactions, J. Phys. Chem. C 114 (2010) 8184–8191, https://doi.org/10.1021/jp100168q.

[68] P.K. Shukla, P.C. Mishra, Effects of diameter, length, chirality and defects on the scavenging action of single-walled carbon nanotubes for OH radicals: a quantum computational study, Chem. Phys. 369 (2010) 101–107, https://doi.org/10.1016/j. chemphys.2010.03.011.

[69] V. Ruiz, L. Yate, I. García, G. Cabanero, H. Grande, Tuning the antioxidant activity of graphene quantum dots: protective nanomaterials against dye decoloration, Carbon 116 (2017) 366–374, https://doi.org/10.1016/j.carbon.2017.01.090.

[70] E. Gazzano, M. Ghiazza, M. Polimeni, V. Bolis, I. Fenoglio, A. Attanasio, G. Mazzucco, B. Fubini, D. Ghigo, Physicochemical determinants in the cellular responses to nanostructured amorphous silicas, Toxicol. Sci. 128 (2012) 158–170, https://doi.org/10.1093/toxsci/kfs128.

[71] P.R. Lockman, J.M. Koziara, R.J. Mumper, D.D. Allen, Nanoparticle surface charges alter blood–brain barrier integrity and permeability, J. Drug Target. 12 (2004) 635–641, https://doi.org/10.1080/10611860400015936.

[72] E. Fröhlich, The role of surface charge in cellular uptake and cytotoxicity of medical nanoparticles, Int. J. Nanomed. 7 (2012) 5577–5591, https://doi.org/10.2147/IJN. S36111.

[73]   V. Sokolova, D. Kozlova, T. Knuschke, J. Buer, A.M. Westendorf, M. Epple, Mechanism of the uptake of cationic and anionic calcium phosphate nanoparticles by cells, Acta Biomater. 9 (2013) 7527–7535, https://doi.org/10.1016/j.actbio. 2013.02.034.

[74]   H.Y. Tan, N. Wang, S. Li, M. Hong, X. Wang, Y. Feng, The reactive oxygen species in macrophage polarization: reflecting its dual role in progression and treatment of human diseases (Article ID 2795090), Oxid. Med. Cell. Longev. (2016) 1–16, https://doi.org/10.1155/2016/2795090.

[75]   H. Kawasaki, A mechanistic review of silica-induced inhalation toxicity, Inhal. Toxicol. 27 (2015) 363–377, https://doi.org/10.3109/08958378.2015.1066905.

[76]   S.S. Iyer, A.A. Ghaffari, G. Cheng, Lipopolysaccharide-mediated IL-10 transcriptional regulation requires sequential induction of type I IFNs and IL-27 in macrophages, J. Immunol. 185 (2010) 6599–6607, https://doi.org/10.4049/jimmunol. 1002041.

[77]   J. Todoric, L. Antonucci, M. Karin, Targeting inflammation in cancer prevention and therapy, Cancer Prev. Res. 9 (2016) 895–905, https://doi.org/10.1158/19406207.CAPR-16-0209.